Received: 2 February 2023 | Revised: 21 April 2023 | Accepted: 28 May 2023

DOI: 10.1002/sus2.139

RESEARCH ARTICLE

SusMat WILEY

Establishment of green graphite industry: Graphite from biomass and its various applications

Ziyi Shi[1] | Shule Wang[1,2] | Yanghao Jin[1] | Lingfeng Zhao[1] | Shiwei Chen[3] | Hanmin Yang[1] | Yuxiao Cui[4] | Rikard Svanberg[1] | Chuchu Tang[5] | Jianchun Jiang[2] | Weihong Yang[1] | Pär G. Jönsson[1] | Tong Han[1]

[1]Department of Materials Science and Engineering, KTH Royal Institute of Technology, Stockholm, Sweden

[2]Jiangsu Co-Innovation Center of Efficient Processing and Utilization of Forest Resources, International Innovation Center for Forest Chemicals and Materials, College of Chemical Engineering, Nanjing Forestry University, Nanjing, China

[3]University of Michigan-Shanghai Jiao Tong University Joint Institute, Shanghai Jiao Tong University, Shanghai, China

[4]Department of Fiber and Polymer Technology, KTH Royal Institute of Technology, Stockholm, Sweden

[5]Faculty of Creative Arts, University of Malaya, Kuala Lumpur, Malaysia

Correspondence
Tong Han, Department of Materials Science and Engineering, KTH Royal Institute of Technology, Stockholm, Sweden.
Email: tongh@kth.se

Funding information
Bio+program; Energimyndigheten-The Swedish Energy Agency, Grant/Award Number: 2021-00048; Teknikområde 23

Abstract

Resource- and energy-efficient biomass exploitation for green graphite production is one of the most effective strategies for satisfying graphite demand while minimizing energy consumption and carbon emissions. This study investigated green graphite production from biomass waste and its applications to establish a green graphite industry. Biomass pyrolysis and catalytic graphitization of biochar were studied first to produce green graphite. The optimized green graphite exhibited a reversible capacity of 264 mA h/g and 97% capacity retention over 100 cycles in a half-cell. Green graphite electrodes with a resistivity lower than 5 $\mu\Omega$ m were fabricated by using organic fraction bio-oil as a green binder. Other green graphite applications, including printing, conductive printing, pencils, and refractories, were also achieved. The overall process of graphite anode and electrode synthesis from biomass waste and short-rotation energy crops was modeled. Approx. 95 kg of battery graphite or 109 kg of metallurgical graphite electrodes can be produced per ton of biomass with low primary energy consumption and carbon footprint. Prominently, the modeling result and life cycle assessment demonstrated that, for the production of battery graphite from biomass waste, net-negative-CO_2 emissions (−0.57 kg CO_2-eq/kg graphite powders) with net-negative-primary energy consumption (−28.31 MJ/kg graphite powders) was achieved.

KEYWORDS
biomass, green graphite, lithium-ion battery anode, metallurgical graphite electrode, negative emission

Ziyi Shi and Shule Wang contributed equally to this work.

1 | INTRODUCTION

Graphite and graphite-based materials, listed as a "strategic and critical mineral" by the U.S. government and the European Union, have key applications in various industries, including batteries and metallurgy.[1–3] Currently, the growing demand of the battery and the increasing use of environmentally friendly electric arc furnaces (EAFs) in emerging countries have contributed to the graphite market's expansion, as illustrated in Figure S1, resulting in a tight supply of graphite and a surge in graphite prices.[4–6]

Today's commercial graphite can be categorized into natural graphite and synthetic graphite. Natural graphite is mined from natural mineral deposits, subjected to geographical restrictions.[7,8] Graphite excavation causes significant environmental damage,[9] and graphite purification involves a series of energy- and chemical-sensitive processes.[10] The energy demand for producing 1 ton of battery-grade natural graphite is estimated to be approximately (approx.) 1.1×10^4 MJ, associated with global warming potential (GWP) of approx. 5.3 t CO_2-equivalence (CO_2-eq) emissions.[11] Another concern regarding natural graphite is the mining sources. The majority of natural graphite powders are currently mined and produced in China and India, which hold 66% and 14% share of total world production, whereas the production of natural graphite powders in Europe is less than 1%.[12] Synthetic graphite, on the other hand, is produced using fossil-based carbon resources as raw materials, and the graphitization process requires ultrahigh temperatures (>2500°C) for several weeks.[13–15] Manufacturing 1 metric ton of graphite (in terms of graphite electrodes) consumes over 4.0×10^4 MJ of energy, with over 10 metric tons of CO_2-eq emissions.[16,17] In short, today's graphite production processes are incredibly energy-intensive, high-carbon footprint, and thus unsustainable. As the world moves toward achieving net-zero emissions, the contradiction between the high demand for high-quality graphite products and its unsustainable production process is increasingly prominent.

Approximately 140 Gt of biomass is generated each year globally. Energy- and resource-efficient biomass utilization as green graphite product precursors can address issues such as graphite supply constraints and high energy consumption and emissions in traditional graphite production processes.[18–20] For decades, scientists have been researching catalytic graphitization to convert amorphous carbon from renewable sources into graphitic carbon.[21,22] So far, most research in this area has focused on developing more efficient catalysts, and corresponding catalytic graphitization processes.[22–24] Although bio-based graphite is primarily used as battery anode material, other potential applications, such as metallurgy and refractory, have not yet been fully explored.[25–27] In addition to solid carbon materials, it is important to consider other products that can be produced from biomass to achieve high resource efficiency. A comprehensive and sustainable approach is currently missing, including a full life cycle assessment (LCA), for producing green graphite from biomass for various applications.

In this study, a tandem biorefinery process that includes biomass pyrolysis, catalytic graphitization of biochar, acid washing, and recycling of the catalyst was developed to produce green graphite in powder. The performance of graphite powders as anode material in lithium-ion batteries was investigated. Thereafter, the green graphite powders were compacted and shaped into electrodes using a portion of the bio-oil as a renewable binder, and a prototype of EAF was constructed by using green graphite electrodes, to demonstrate its potential for application in the metallurgical industry. Additionally, the study also explored other potential applications of green graphite, such as pencil leads, refractories, and conductive inks. In the end, the study evaluated the overall process under different scenarios where the bio-oil and gas derived from the pyrolysis process were utilized as energy sources and determined the cumulative energy demands (CEDs) and GWPs of the process.

2 | RESULTS AND DISCUSSION

2.1 | Biomass pyrolysis and catalytic graphitization of biochar to produce green graphite

2.1.1 | Biomass pyrolysis

This work started with the biomass pyrolysis process, followed by the catalytic graphitization of biochar to produce graphite, as illustrated in Figure 1A. A pilot-scale continuous biomass pyrolysis process was considered, which resulted in the production of solid biochar (20.6 wt.%), organic fraction bio-oil (OFB, 9.85 wt.%), aqueous fraction bio-oil (AFB, 32.1 wt.%), and gas (37.0 wt.%), as depicted in Figure 1B. For liquid, OFB and AFB were separated by gravity. The elemental compositions and corresponding water content of OFB and AFB are listed in Table S1, whereas the specific chemical composition of OFB and gas is presented in Table S2 and Figure S2. From an energy perspective, OFB, AFB, and gas have high heating values of 27.77, 4.64, and 14.36 MJ/kg, respectively (Figure 1B), which indicated that the process could coproduce other green fuels apart from biochar, which is employed as graphite precursor. From an element perspective, biochar is a carbon-rich product with an H/C atomic ratio of

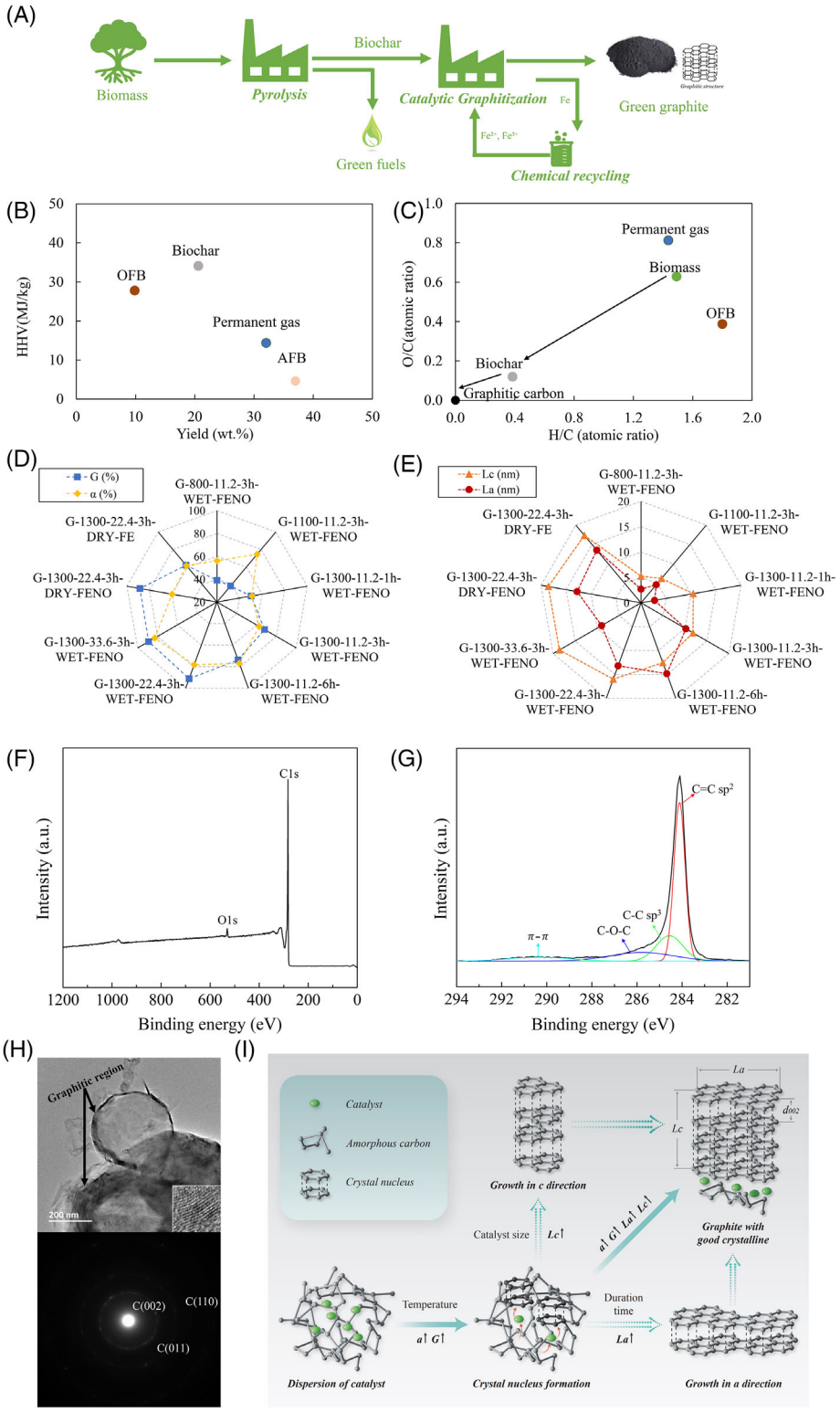

FIGURE 1 (A) Schematic diagram of the biomass pyrolysis and catalytic graphitization of biochar process; (B) yield versus higher heating value (HHV) of pyrolysis products obtained after a continuous biomass pyrolysis test; (C) atomic O/C–H/C ratios of raw biomass and pyrolysis products (Permanent gas, HFBO, and biochar); (D) calculated L_c and L_a values versus catalytic graphitization process parameters; (e) calculated G and α values versus catalytic graphitization process parameters; (F) a full-scan XPS spectra of G-1300-22.4-WET-3h-FENO sample; (G) C1s high-resolution XPS spectra of G-1300-22.4-WET-3h-FENO sample; (H) transmission electron micrographs of G-1300-22.4-WET-3h-FENO sample with the selected area electron diffraction (SAED) pattern; (I) proposed mechanism for the evolution of graphitic crystalline during catalytic graphitization process.

approximately one quarter of biomass and an O/C atomic ratio of approximately a fifth of biomass, indicating a promising precursor of graphite with H/C and O/C atomic ratios close to zero (Figure 1C).

2.1.2 | Catalytic graphitization of biochar

Iron-based catalysts were selected for the catalytic graphitization of biochar due to their good catalytic performance,[25,27,28] earth-abundance,[29] and low cost.[30] In this work, a systematic study was conducted on the iron catalyst's influence and the processing parameter on the graphite crystalline property. Figure S3 shows that the X-ray diffraction (XRD) pattern of untreated biochar had an amorphous carbon structure, whereas that of all graphite products performed a typical graphitic structure with intensity shifts corresponding to different graphitic crystal planes. In addition, as illustrated in Figure S4, the Raman spectroscopy for graphite displayed a much higher G-shift intensity but a much lower D-shift intensity than untreated biochar. Graphite crystal characterization parameters (i.e., d_{002}, $G\%$, L_c, and L_a) as well as the conversion rate from amorphous carbon to graphitic carbon (i.e., α) were calculated based on the XRD and Raman spectra (Table S3). These characterization parameters are summarized in Figure 1E,E. It was observed that when $Fe(NO_3)_3$ catalyst was incorporated into biochar via the wet impregnation method, the $G\%$, L_c, and α values of the graphite samples positively correlated with the graphitization temperature and duration time. The L_c and α values of those samples also had a positive correlation with the catalyst loading amount. However, the $G\%$ value of the graphite reached a maximum at a catalyst loading of 22.4 wt.%. When $Fe(NO_3)_3$ and Fe catalysts were added to biochar via the dry impregnation method (1300°C, 22.4% iron loading, 3 h), relatively low $G\%$ and α values were obtained, whereas the L_c value of the graphite sample was slightly higher than the G-1300-22.4-WET-3h-FENO sample. It turned out that, regardless of the catalyst type, loading, and addition method, graphite samples that were produced using longer graphitization duration time and higher graphitization temperature always had higher L_a values. In addition, the results indicated that the L_a value was more sensitive to the duration time instead of temperature. Moreover, compared with the dry impregnation method, the wet impregnation method led to smaller catalyst particle sizes but higher dispersion degrees of the catalyst. For the wet impregnation method, an increase in catalyst loading caused an increase in the catalyst particle size. All these can be verified in Figure S5. These results indicated that good catalyst dispersion was favorable for increasing $G\%$ and α values, and a relatively large catalyst particle size was favorable for high L_c values.

The XPS spectra of the G-1300-22.4-WET-3h-FENO sample are presented in Figure 1F. As can be seen in the figure, only the signals from C and O elements were detected in the full-scan XPS spectra. Figure 1G shows the C1s XPS spectra and the resulting curves fit for C–C, C=C, C–O–C, and π–π. The characteristic peaks of C=C and π–π suggested a highly ordered graphitic structure in the graphite sample. TEM, in conjunction with the selected area electron diffraction pattern of the G-1300-22.4-WET-3h-FENO sample, as shown in Figure 1G, also verified the existence of graphitic crystalline.

Generally, two kinds of mechanisms for catalytic graphitization have been extensively studied and admitted: (i) dissolution–precipitation and (ii) metal carbide formation–decomposition. Dissolution–precipitation is believed to be the primary mechanism in this work due to the good solubility of carbon in iron.[21] Our results suggested that, apart from the influence of the temperature, the uniform dispersion of the catalyst could also contribute to a high degree of graphitization ($G\%$) and a high conversion rate (α). The uniform dispersion of catalysts could increase the contact between the catalyst and carbon,[21,31] resulting in a great number of active sites for dissolution–precipitation, and the enhanced formation of the graphitic nanocrystals. As shown in TEM in Figure 1H, the annular graphitic domains suggested the graphitic nanocrystals surrounding the iron catalyst were formed via the dissolution–precipitation mechanism at the initial stage.

However, this mechanism seems to be responsible for the initial stage of catalytic graphitization, but it is difficult to explain the growth of graphite crystals throughout the catalytic graphitization process. It turned out that a relatively large catalyst particle size could induce a relatively high graphitic crystal stacking height (L_c). Moreover, the extension of the graphitization duration was found to be most favorable for the growth of the graphitic crystal size (L_a). In this study, a mechanism of crystal nucleation and growth was proposed to describe the growth of graphitic crystalline during the catalytic graphitization process, as shown in Figure 1I. The mechanism is also commonly used in metallurgy to explain graphite nucleation and growth in liquid metals.[32,33] At the onset of catalytic graphitization, crystal nuclei were formed according to the dissolution–precipitation mechanism between carbon and Fe.[21,23] In the presence of catalysts at high temperatures, this nucleus grew in "*a*" (graphite crystal plane extension) and "*c*" (graphene layer stacking) directions to form a larger graphite crystalline structure. High dispersion of iron catalyst favored the formation of the crystal nucleus, which resulted in relatively high $G\%$ and α values. Larger

catalyst particle sizes promoted the growth in the "*c*" direction (an increase of L_c), and the extending duration time boosted the growth in the "*a*" direction (an increase of L_a).

2.1.3 | Catalyst removal and recycling

Acid washing of the sample was performed to remove and recycle the iron catalyst embedded into carbon during catalytic graphitization of biochar. According to Figure 2A, α-Fe was the major resulting state of the catalyst after the graphitization process. In addition, iron carbide was also detected in the sample. Specifically, a two-step washing method was employed, with the first step involving washing in hydrochloric acid (HCl). The influence of the acid concentration and treatment temperature on the iron catalyst removal efficiency was studied, as shown in Figure 2B. The result revealed that increasing the HCl concentration improved the catalyst removal efficiency. At 60 and 80°C, the catalyst removal efficiency increased from 97.29% to 98.33% and from 98.34% to 98.59%, respectively. Figure 2C shows that the color of the spent solutions deepened with increasing temperature and HCl concentration due to enhanced oxidation. Below 80°C, a higher temperature was found to be more effective than a higher acid concentration for iron catalyst removal. However, at a higher temperature of 80°C, an increase in the acid concentration was more effective for catalyst removal. A concentration of 1 mol/L HNO_3 at 80°C was confirmed to be the optimal condition based on both the iron catalyst removal efficiency and the HCl utilization efficiency. Dissolved iron salts in spent HCl solutions could be recycled and used as catalysts for the graphitization process, which is essential to establish a sustainable graphite production process. Theoretically, the catalyst recycling efficiency could be 98%, equal to the iron catalyst removal efficiency. In practical recycling trials, an iron recycling rate of approx. 90% was achieved, as illustrated in Figure 2D. To meet the low ash requirement of advanced applications such as batteries, the second step that consisted of microwave-assisted digestion with *aqua regia* was subsequently performed to further decrease the iron content. The process further reduced the average Fe mass content to 0.2 wt.%, as shown in Figure 2D. SEM photos revealed that purified graphite particles existed as flakes with a particle size distribution ranging between 1 and 100 μm, as shown in Figure 2E. The morphology of the green graphite powder did not have distinct differences from that of raw biochar powder, which was attributed to the graphitization process occurring on a microscopic level.[34] The corresponding energy-dispersive spectroscopy mapping micrographs of unwashed and ultimate (washed) samples cleared confirmed the removal of the iron catalyst (Figure 2E-5–8).

2.2 | Application of green graphite as anode material for lithium-ion batteries

The anode of a lithium-ion cell is predominantly made of graphite, constituting 15%–30% of the total cell mass and 11%–23% of the total cell manufacturing cost ($10–$20 per kg).[35] The production of high-quality green graphite powers as anode materials for lithium-ion batteries was one of the main motivations behind this study. A schematic diagram of the battery assembling process using green graphite as an anode material is shown in Figure 3A.

In this work, the optimized graphite sample, G-1300-22.4-WET-3h-FENO, was selected for electrochemical evaluation in a coin-type half-cell. Figure 3B,C shows galvanostatic charge–discharge profiles, and long-cycle stability plots were obtained at a current density of 25 mA for 100 cycles. The graphite sample displayed an initial discharged and charged capacity of approx. 382 and 257 mA h/g, corresponding to an initial coulombic efficiency of 67%. Although the ICE value is lower than that of current-use battery graphite (~100%), it is comparable to that reported in the literature for graphite samples (55%–90%).[25,36] The capacity loss is attributed to the reduction of electrolytes and the formation of stable solid-electrolyte interphase (SEI) layer. The irreversibility of the SEI formation is well supported by the disappearance of the cathodic peaks originating from SEI formation reactions in subsequent cycles. The significant SEI formation is strongly correlated to the relatively abundant electrolyte-accessible edge/defect surface areas of the graphite sample detected by the nitrogen adsorption–desorption measurement.[37] Figure S6 indicates that the BET (Brunauer, Emmett, and Teller) surface area of the graphite sample was 70 m^2/g, much higher than the commercial battery-use graphite (5–20 m^2/g).[38] After the first ~5 cycles, the stable SEI layer and the activation of the electrode were achieved with CE increasing to above 99%. The reversible capacity of the graphite sample was sable at approx. 264 mA/g, which was slightly lower than the value reported in the literature (~ 300 mA h/g).[25,36] But the capacity retained approx. 97% after 100 cycles with CE higher than 99.3%, which is superior to that of green graphite samples in the literature.[25,36] As shown in Figure 3D, the cyclic voltammetry of the first-to-fifth cycles demonstrated the electrochemical reversibility of the green graphite. Furthermore, the rate capacity of the green graphite sample was tested to assess the reversible capacity at a high charging rate. As plotted in Figure 3E, the specific reversible capacity values of 267, 259, 246, and 223 mA h/g were observed at charging rates of 25, 50, 100, and 200 mA/g, respectively. The result indicated that the green graphite sample exhibited reasonable capacity reduction at high charging rates as well as outstanding capacity self-recovery.

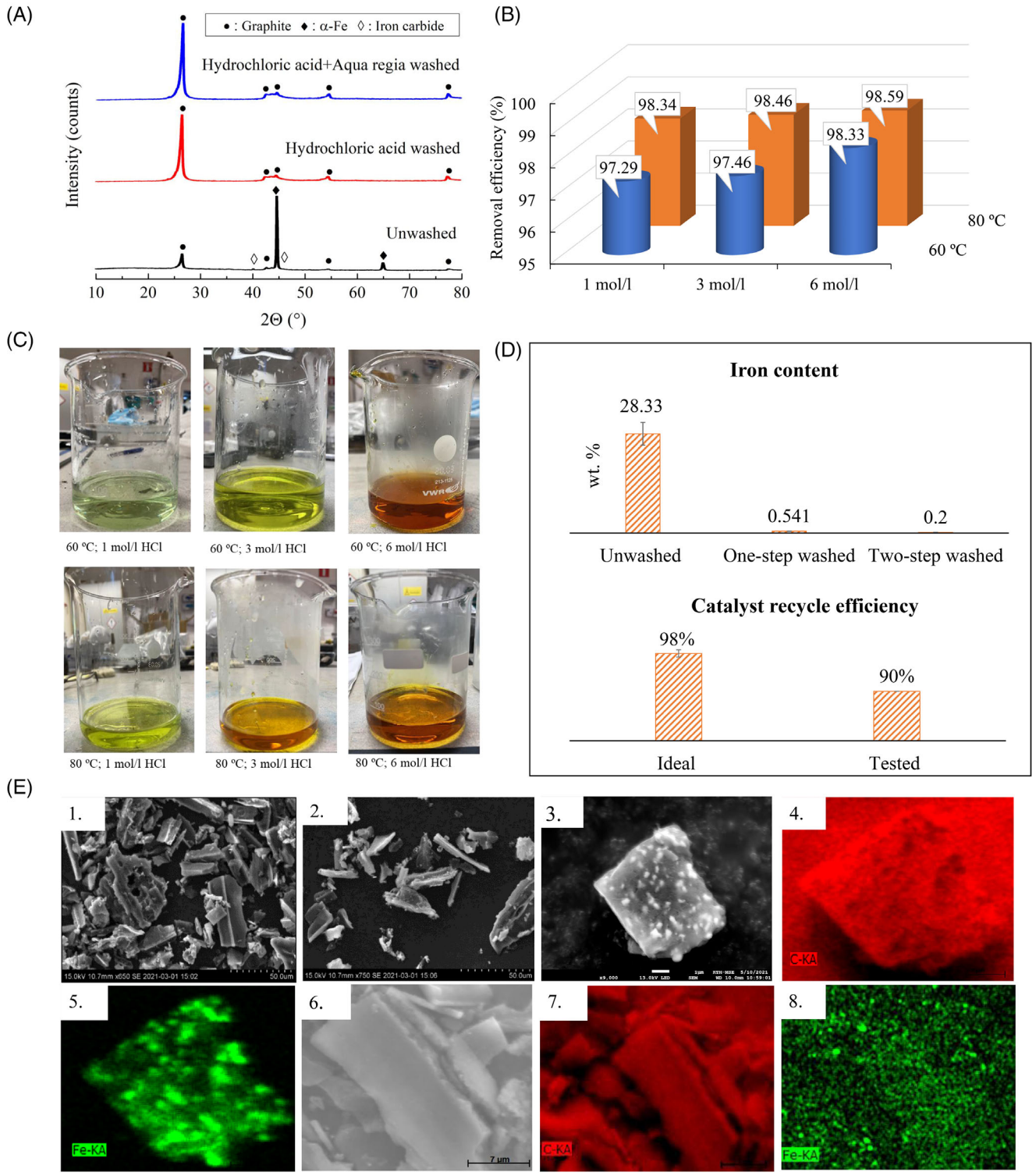

FIGURE 2 (A) X-ray diffraction (XRD) patterns of unwashed, nitric acids washed and nitric acids+ Aqua regia washed G-1300-22.4-wet-3h-FENO samples; (B) catalyst removal efficiency at different acid washing conditions; (C) photographs of the liquid collected after the first step of HCl washing; (D) iron content of unwashed samples, samples after one-step washed, and samples after two-step washed and corresponding catalyst recycle efficiency; (E) EDS mapping of unwashed and ultimate (after the two-step washed) G-1300-22.4-wet-3h-FENO samples: e-1, overall SEM of unwashed graphite particles; e-2, overall SEM of ultimate graphite particles; e-3, SEM of unwashed graphite particles; e-4, distribution of carbon elements on unwashed graphite particles; e-5, distribution of Fe elements on unwashed graphite particles; e-6, SEM of ultimate graphite particles; e-7, distribution of carbon elements on ultimate graphite particles; e-8, distribution of Fe elements on ultimate graphite particles.

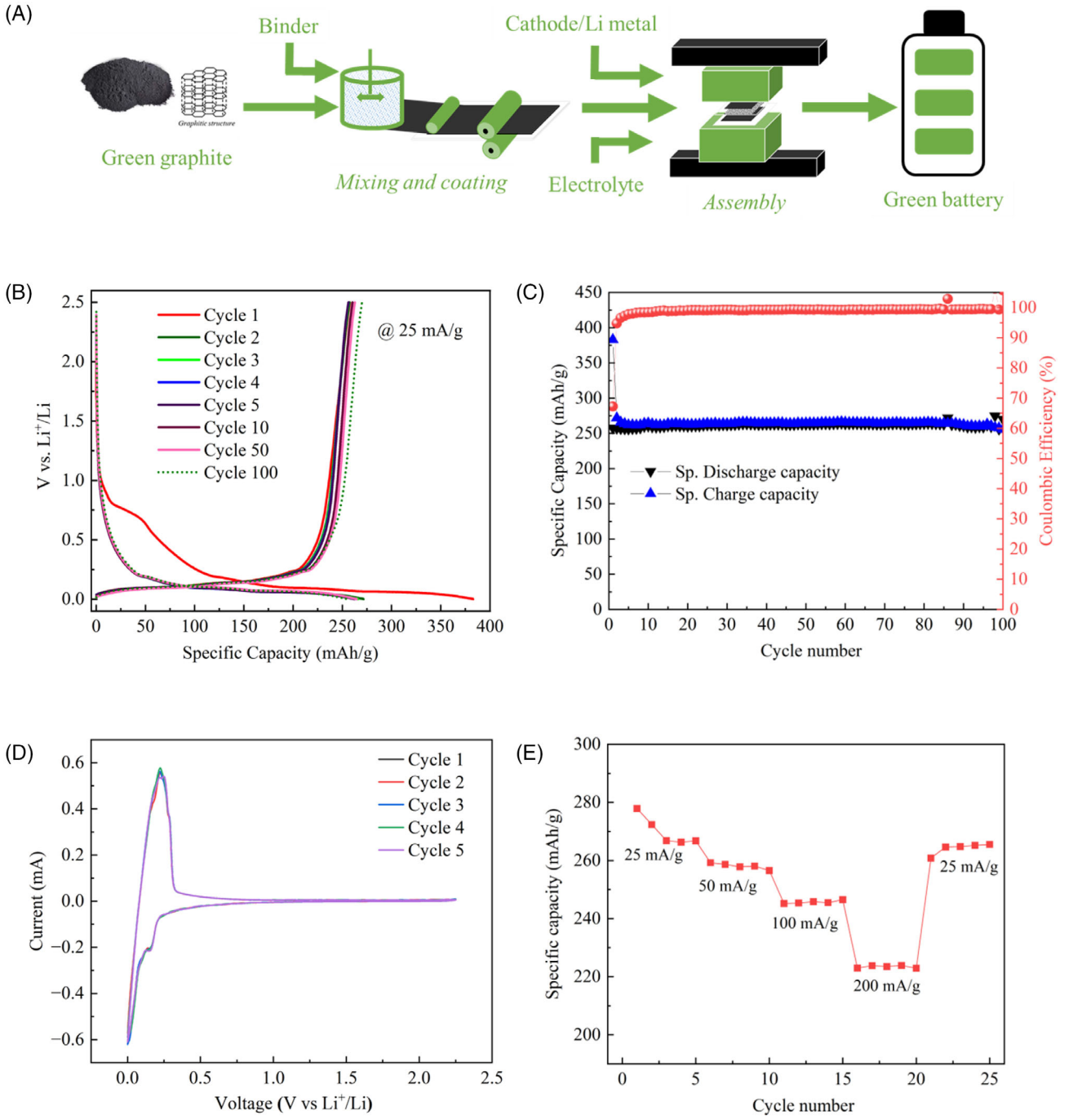

FIGURE 3 (A) Schematic diagram of the green battery assembly process using green graphite as anode material; (B) galvanostatic charge–discharge profiles of green graphite in half-cells; (C) cycling performance of green graphite in half-cells; (D) current–voltage curve of green graphite in halt cells; (E) rated capacity of the green graphite in half-cells.

In summary, the green graphite sample was found to be a viable anode material for lithium-ion batteries, with electrochemical properties comparable to those of graphite samples reported in the literature. Although there is still a slight gap compared to commercial battery-grade graphite, these results manifest the potential of green graphite in energy storage applications.

2.3 | Graphite electrodes prototype fabrication and application

2.3.1 | Development of a green binder

As shown in Figure S1, graphite electrodes used in metallurgy industries are expected to be one of the largest

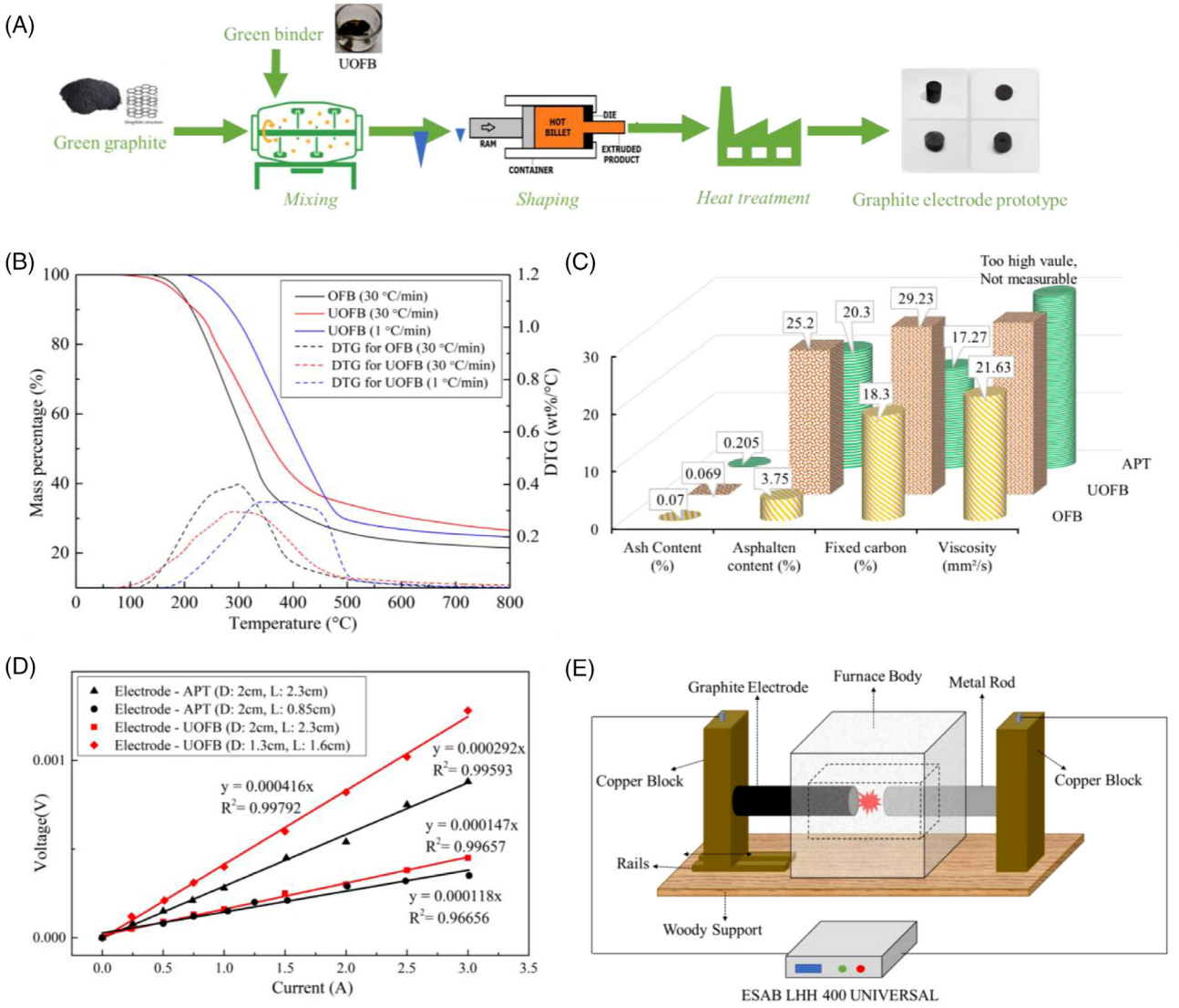

FIGURE 4 (A) Schematic diagram of the graphite electrode production process; (B) TGA curves of organic fraction bio-oil (OFB) and upgraded OFB (UOFB); (C) characterization results of binders; (D) *I–V* curves of representative graphite electrodes and calculated resistivity values; (E) schematic diagram of the electric arc furnace (EAF) prototype.

downstream markets of graphite within the next 10 years. In this study, graphite electrodes were fabricated from the produced green graphite powders following the production process outlined in Figure 4A. In this process, a green binder was developed first to make the entire graphite electrode production process fossil-free. OFB usually has high viscosity (>1 mm^2/s) as well as the possibility of being used as a binder for graphite powder shaping.[39] However, the first attempt of OFB as a binder to fabricate graphite electrodes failed due to its relatively lower viscosity (Table S4). Aging OFB by heat treatment has been reported to be effective in increasing bio-oil viscosity.[40] To overcome the issue of low viscosity, OFB was subjected to a 72-h heat treatment at 80°C. Figure S7 shows, after heat treatment, the upgraded OFB (UOFB) was transformed into a solid form rather than liquid as OFB at room temperature. TGA and other characterization results, as shown in Figure 4B,C, illustrated that UOFB performed much higher asphaltene content (from 3.75% to 25.2%), fixed carbon (from 18.3% to 29.23%), and viscosity (from 21.63 mm^2/s to a too high value not measurable) than OFB. Moreover, all these values of UOFB were comparable with those of Asphalt (APT), which was applied as a commercial binder. All these findings indicated that UOFB could serve as an appropriate binder for graphite electrode fabrication.

2.3.2 | Graphite electrode fabrication

The successful fabrication of the graphite electrodes using UOFB as a binder is shown in Figure 4A. For compari-

son, APT was also used as a binder for graphite electrode fabrication. To fabricate compact and well-shaped graphite electrodes with good resistivity, a systematic study was conducted to determine the optimal binder-to-graphite powder ratio, the final heat treatment temperature, and the corresponding heating rate. The results are summarized in Table S4. A binder-to-graphite powder ratio of 30–35 wt.%, heating rate above 50°C/min, and final heating treatment temperature of 1300°C were verified to be essential for fabricating compact and well-shaped graphite electrodes. Graphite electrodes not prepared with the above parameters were either in powders, shaped but deformed (seen in Figure S8), shaped but fragile (seen in Figure S9), or highly resistive (>1500 $\mu\Omega$ m).

Compact and well-shaped graphite electrodes (using either UOFB or APT as a binder) all exhibited a resistivity lower than 5 $\mu\Omega$ m (seen in Figure 4D and Table S5), which is comparable to commercial graphite electrodes.[41] OFB, especially UOFB, was mainly composed of phenolic substances derived from lignin decomposition,[42] and the coke generated after the carbonization of these compounds contained non-graphitic hard carbon.[43] Nevertheless, our results indicated that the existence of a certain amount of hard carbon did not significantly affect the resistivity of the graphite electrode. One possible explanation could be either the relatively low amount of hard carbon being left after a subsequent heating treatment or the good conductivity of the bio-oil-derived hard carbon.[44] Previous studies have shown that hard carbon produced from biomass via high-temperature treatment had good electrical conductivity due to the existence of graphene layers.[45]

2.3.3 | Application of graphite electrodes

Thereafter, we constructed a prototype of EAF to demonstrate the use of graphite electrodes in metallurgy industries. A completely renewable graphite electrode fabricated by using green graphite powders and UOFB was used. The schematic figure of the EAF can be seen in Figure 4E. As illustrated in Video S1, the EAF produced a steady arc when both electrodes were graphite electrodes. Real metal melting tests were carried out by replacing one of the graphite electrodes with pure metal, that is, Cu, Al, and Fe. The melting process was recorded in Video S2. Based on the lab-scale melting tests, Figure S10 shows that approximately 1.2, 11, and 49 kg of graphite electrodes (UOFB binder) were consumed to melt 1 metric ton of Cu, Al, and steel, respectively. All these results indicated a promising potential of the produced graphite electrodes in the metallurgical application.

2.4 | Other application

Other applications of green graphite powders were explored in this section. As illustrated in Figure 5A, the green graphite powders were successfully used for the preparation of inks and pencil leads. The inks synthesized by mixing the fine green graphite powders (<80 μm) with OFB (seen in Figure 5B) were used as normal and conductive inks to produce normal printing and conductive circuits (length in a total of 26 cm, width of 0.5 cm), shown in Figure 5C,D. Successful lighting of the LED light confirmed the continuity of the circuit, and the resistance value of the circuit was measured to be 1.3 Ω/cm (Table S5). Pencil leads were also produced successfully from green graphite powders. The preparation process of pencil lead is very similar to that of graphite electrodes, except that clay is used as the binder for pencil lead production instead of UOFB. Figure 5E,F shows examples of pencil leads and the corresponding writing. At last, as shown in Figure 5G, high-temperature thermal shock testing was conducted to evaluate the refractory performance of the green graphite. The green graphite electrode prototype produced in Section 2.2 was used for testing. After exposure to a high-temperature flame of above 1000°C for 3 min, no obvious damage or collapse of the graphite block was observed, indicating that the green graphite products also have the potential to be applied in refractory production.

2.5 | Process model design and evaluation

2.5.1 | Mass and energy balance

Based on the experimental results, the overall process models were designed, modeled, and evaluated. Considering that the major markets for graphite are batteries and metal processing, two process models were developed. Model I aimed to produce graphite powders for batteries (battery graphite), and Model II intended to produce graphite electrodes for metallurgy (metallurgical graphite electrodes). A detailed description of the two models can be seen in Figure 6A. For highly efficient utilization of biomass, coproducts generated from biomass pyrolysis, including OFB (either fully or partially), AFB, and gas, were used for internal energy supply and excess energy export through combined heat and power generation (CHP). The generated heat and power were assumed to furnish the heat and power required within the process.

The mass flows of the two models are shown in Figure 6B,C, respectively. Results indicated that for Model

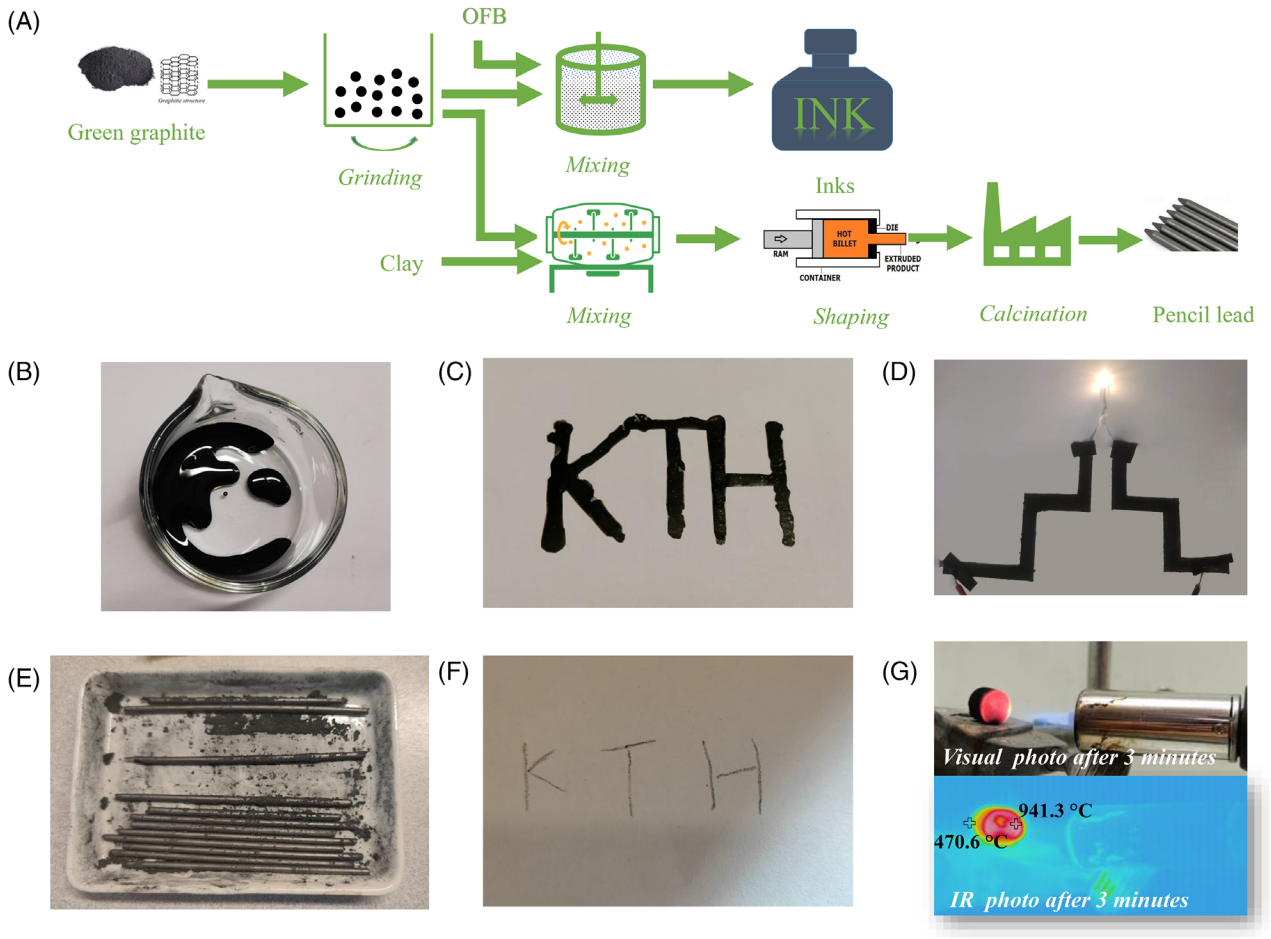

FIGURE 5 (A) Schematic diagram of green inks and pencil lead production from green graphite; (B) appearance of prepared inks; (C) photo of normal printing example; (D) photo of conductive circuit example; (E) photo of pencil leads; (F) photo of writing example using pencil leads; (G) photo of high-temperature thermal shock testing using graphite electrodes.

I, approx. 95 kg of graphite powders could be produced per ton of biomass. In addition, for Model II, approx. 109 kg of graphite electrodes could be produced per ton of biomass. Approx. 327 kg of AFB, 340 kg of gas, and 103 kg of OFB were coproduced per ton of biomass in Model I, which could generate approx. 4960 MJ of electricity and 2056 MJ of heat. In addition, approx. 327 kg of AFB, 340 kg of gas, and 56 kg of OFB were coproduced per ton of biomass in Model II, generating approx. 2055 MJ of electricity and 4274 MJ of heat. Specifically, in both models, the energy required by the grinding, graphitization, and shaping (only in Model II) was assumed to be supplied by the generated electricity. The energy required by the rest units, including pyrolysis and drying, was designed to be provided by the generated heat. The excess heat was recognized as waste heat for a conservative estimation, and the excess electricity was exported to the grid as an alternative to the electricity produced from other sources.

2.5.2 | Life cycle assessment (LCA)

The driving force behind using renewable biomass as an alternative to fossil resources for graphite production is to achieve a lower carbon footprint. In this study, we evaluated the environmental impact of the proposed process models through an LCA study in which the CED and the GWP were calculated. As illustrated in Figure 6A, four scenarios were considered: Scenarios 1 and 2 referred to the production process of graphite products from industrial-available biomass waste, that is, sawdust in this study. For scenarios 3 and 4, the energy crops were involved in graphite production instead of biomass waste, requiring the inclusion of biomass cultivation and harvesting into the overall process. Scenarios 3 and 4 extended the viability of establishing a green graphite industry to regions where biomass is scarce.

CEDs for each process model under different scenarios can be found in Figure 6D. To produce 1 kg of battery-use

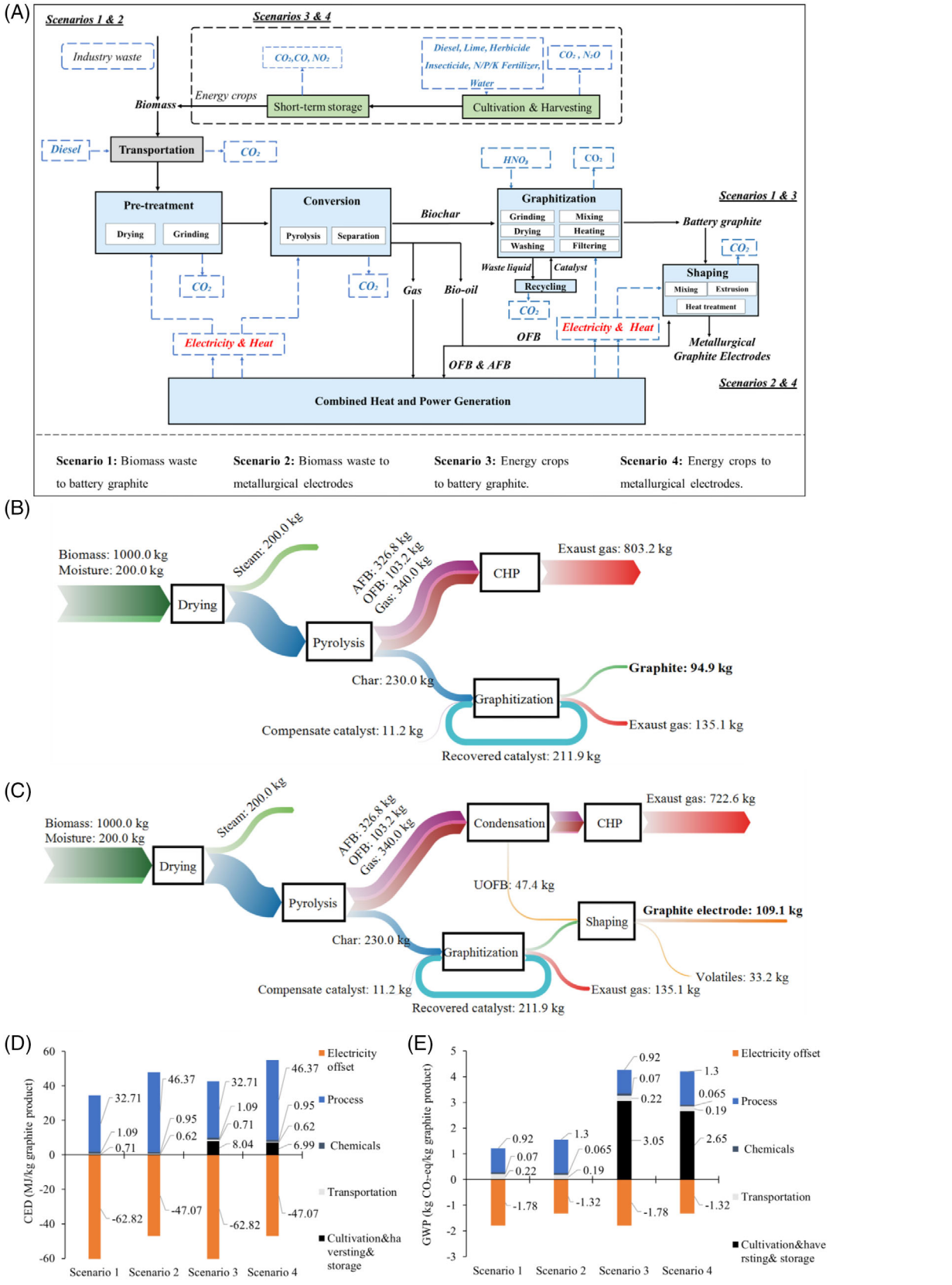

FIGURE 6 (A) Scope of the process model and boundary clarification of the life cycle assessment (LCA) study; (B) mass flow for process model that produces graphite for battery; (C) mass flow for process model that produces graphite electrodes for metallurgy; (D) calculated cumulative energy demand (CED) values of process under different scenarios; (E) calculated global warming potential (GWP) values of process under different scenarios.

graphite powders from biomass waste, 34.51 MJ of cumulative energy was required, comprising 32.71 MJ for process, 1.09 MJ for chemical production, and 0.71 MJ for transportation. Meanwhile, 62.82 MJ could be produced from the CHP unit, resulting in a CED of −28.31 MJ/kg graphite powders (scenario 1, a negative CED referred to that the process has the potential to produce more energy than it consumes), whereas to produce 1 kg of graphite electrodes, 47.94 MJ (46.37 MJ for process, 0.95 MJ for chemical production, and 0.62 MJ for transportation) was required, with 47.07 MJ of energy produced from the CHP unit. The net CED of the process was 0.87 MJ/kg graphite electrodes (scenario 2). Compared with the production of battery-use graphite powders, the production of graphite electrodes has higher energy consumption and lower energy compensation, mainly due to the deployment of forming process and the consumption of partial OFB as the binder. For scenarios 3 and 4, biomass cultivation, harvesting, and storage led to extra CEDs of 8.04 MJ/kg graphite powders and 6.99 MJ/kg graphite electrodes. As a result, the CEDs of graphite powders production and electrode production from energy crops were estimated to be −20.27 MJ/kg graphite powders (scenario 3) and 7.86 MJ/kg graphite electrodes (scenario 4).

GWPs for each process model under different scenarios are presented in Figure 6E. In scenario 1, the production of 1 kg of battery graphite from biomass waste emitted 1.21 kg of CO_2-eq (0.92 kg from process, 0.07 kg from chemicals, and 0.22 kg from transportation). Generated electricity from the CHP unit could offset the emission of 1.78 kg CO_2-eq/kg graphite powders, leading to a net GWP of −0.57 kg CO_2-eq/kg graphite powders (scenario 1). In scenario 2, 1.59 kg CO_2-eq/kg graphite electrodes (1.3 kg from process, 0.07 kg from chemicals, and 0.19 kg from transportation) were estimated to be emitted, with an emission offset of 1.32 kg CO_2-eq/kg graphite electrodes. The net GWP of scenario 2 was 0.27 kg CO_2-eq/kg graphite electrodes. In comparison with scenario 1, the higher GWP in scenario 2 was attributed to the higher energy consumption of the shaping process and lower emission offset resulting from the binder consumption. For scenarios 3 and 4, biomass cultivation, harvesting, and storage gave rise to extra GWPs of 3.05 kg CO_2-eq/kg graphite powders and 2.65 CO_2-eq/kg graphite electrodes, respectively. Consequently, the net GWPs of graphite powders production and graphite electrode production from energy crops were 2.48 kg CO_2-eq/kg graphite powders (scenario 3) and 2.89 kg CO_2-eq/ kg graphite electrodes (scenario 4).

To summarize, the process in scenario 1 (from biomass waste to battery-use graphite powders) was found to be the most energy-efficient, accompanied by a net reduction in CO_2-eq emissions. The process in scenario 2 (from biomass waste to metallurgical electrodes) showed very low CED and GWP, which are negligible compared to the commercial process. Additionally, scenarios 3 and 4 manifested that using energy crops as raw materials induced a minor change in CED but an obvious increase in GWP. Combining the analysis from four scenarios, it turned out that using industrial biomass waste as raw material was more sustainable in terms of energy and environmental impact than using energy crops. Nonetheless, it is worth noting that all the processes outlined in the four scenarios exhibited significantly lower CEDs and GWPs than the current natural and synthetic graphite production processes.

3 | CONCLUSION

This study investigated the production of green graphite from biomass waste and its various applications for establishing a complete green graphite industry. Specifically, a tandem process that includes biomass pyrolysis, catalytic graphitization of biochar, acid washing, and recycling of the catalyst was first developed to produce green graphite. Thereafter, this study explored the application of green graphite powders as anode material for lithium-ion batteries and further shaped the green graphite powders by using a portion of the bio-oil as a renewable binder to produce green graphite electrodes. Moreover, other small-scale applications using graphite, such as pencil leads, refractories, and printing, have also been examined. Finally, the overall process was designed, modeled, and evaluated under different scenarios.

In the catalytic graphitization of biochar tests, the relationship between the graphite product properties (including crystallite size, degree of graphitization, and graphite morphology) and the graphitization process parameters (iron catalyst type, catalyst loading, temperature, and duration) was clarified. Subsequently, the electrochemical performance of the optimized green graphite sample was determined by assembling half-cells (ICE of 67% and reversible capacity of 264 mA/g). In long-term cycling tests, the capacity was retained approx. 97% after 100 cycles with CE higher than 99.3%. A green binder was developed during the graphite electrode fabrication attempts to create a fossil-free process for graphite electrode production. Graphite electrodes with resistivities lower than 5 $\mu\Omega$ m were successfully fabricated by using the developed green binder. Furthermore, other green graphite products, including normal and conductive ink preparation, pencil leads production, and refractories were also successfully achieved.

Overall process modeling and LCA study indicated that approx. 95 kg of battery-use graphite powders accompanied by 4960 MJ of electricity and 2056 MJ of heat, or 109 kg of metallurgical graphite electrodes

accompanied by 2055 MJ of electricity and 4274 MJ of heat were estimated to be produced per ton of biomass. When using both biomass waste and energy crops as raw materials, the processes' CEDs and GWPs were found to be significantly lower than those of current natural and synthetic graphite production processes. The process of producing battery-use graphite powders from biomass waste was found to have net-energy-exporting capabilities (−28.31 MJ/kg graphite powders) and net-negative-CO_2 emissions (−0.57 kg CO_2-eq/kg graphite powders).

AUTHOR CONTRIBUTIONS

Conceptualization: Tong Han, Weihong Yang. *Methodology*: Ziyi Shi, Shule Wang, Yanghao Jin, Lingfeng Zhao, Shiwei Chen, Hanmin Yang, Yuxiao Cui, Rikard Svanberg, Tong Han. *Investigation*: Ziyi Shi, Shule Wang, Tong Han. *Visualization*: Ziyi Shi, Shule Wang, Yanghao Jin, Lingfeng Zhao, Shiwei Chen, Hanmin Yang, Yuxiao Cui, Rikard Svanberg, Tong Han. *Funding acquisition*: Tong Han, Weihong Yang. *Project administration*: Weihong Yang, Pär Jönsson. *Supervision*: Tong Han, Weihong Yang, Pär Jönsson. *Writing—original draft*: Ziyi Shi, Shule Wang, Tong Han. *Writing—review and editing*: Ziyi Shi, Shule Wang, Yanghao Jin, Lingfeng Zhao, Shiwei Chen, Hanmin Yang, Yuxiao Cui, Rikard Svanberg, Tong Han, Weihong Yang, Pär Jönsson.

ACKNOWLEDGMENTS

We thank Envigas AB for providing the raw biochar products and Elkem carbon AS for test supporting. We also thank James Shipley and Marco Ravana from Quintus AB for shaping consulting and supporting. Funding: The work was funded by Bio+program from Energimyndigheten- The Swedish Energy Agency (project: 'Fossilfri grafit', project number: '2021-00048') and Teknikområde 23 (TO 23) Metallurgy program from Jernkontoret- The Swedish Iron and Steel Industry. Shule Wang and Hanmin Yang would also like to acknowledge funding from the Chinese Scholarship Council (CSC). Tong Han (Posdoc) would like to acknowledge funding from the Research Initiative on Sustainable Industry and Society (IRIS) program from KTH Royal Institute of Technology. The funding from the College of Chemical Engineering, Nanjing Forestry University for proofreading is also appreciated.

CONFLICT OF INTEREST STATEMENT

The authors declare no conflict of interest.

DATA AVAILABILITY STATEMENT

All data needed to evaluate the conclusions in the paper are present in the paper and/or the Supporting Information. Additional data related to this paper may be requested from the authors.

ORCID

Tong Han https://orcid.org/0000-0002-7929-5985

REFERENCES

1. Commission E, Directorate-General for Internal Market, Industry E and Sme. *Study on the review of the list of critical raw materials : critical raw materials factsheets*. Publications Office; 2017.
2. Wan S, Chen Y, Fang S, et al. High-strength scalable graphene sheets by freezing stretch-induced alignment. *Nat Mater*. 2021;20(5):624-631.
3. Li P, Yang M, Liu Y, et al. Continuous crystalline graphene papers with gigapascal strength by intercalation modulated plasticization. *Nat Commun*. 2020;11(1):1-10.
4. Demand for critical raw materials in EVs. Published November 17, 2020. Accessed June 15, 2022. https://www.iea.org/articles/demand-for-critical-raw-materials-in-evs
5. Iron and Steel Technology Roadmap. Published October, 2020. Accessed June 15, 2022. https://www.iea.org/reports/iron-and-steel-technology-roadmap
6. Wood Mackenzie. IMO 2020, EVs, and steel—a perfect storm in the needle coke sector?. Published May 30, 2019. Accessed June 15, 2022. https://www.mining.com/web/imo-2020-evs-steel-perfect-storm-needle-coke-sector
7. Pierson HO. Handbook of carbon, graphite, diamonds and fullerenes: processing, properties and applications. Published May, 2015. Accessed June 15, 2022. https://chemistlibrary.files.wordpress.com/2015/05/handbook-of-carbon-graphite-diamond-and-fullerenes-1993-pierson.pdf
8. Kalyoncu RS, Taylor Jr HA. Natural graphite. *Kirk-Othmer Encycl Chem Technol*. 2000:1-21
9. Companies respond to questions of graphite pollution. Published October 2, 2016. Accessed June 15, 2022. https://www.washingtonpost.com/business/economy/2016/10/02/c9c22ef6-7b7c-11e6-bd86-b7bbd53d2b5d_story.html
10. Kaya Ö, Canbazoğlu M. Chemical demineralization of three different graphite ores from Turkey. *Miner Metall Process*. 2009;26(3):158-162.
11. Gao SW, Gong XZ, Liu Y, Zhang QQ. Energy consumption and carbon emission analysis of natural graphite anode material for lithium batteries. *Mater Sci Forum*. 2018;913(2010):985-990.
12. Jara AD, Betemariam A, Woldetinsae G, Kim JY. Purification, application and current market trend of natural graphite: a review. *Int J Min Sci Technol*. 2019;29(5):671-689.
13. Wood A. Carbon and Graphite. *Concise encyclopedia of advanced ceramic materials*. Elsevier; 1991:57-62
14. Lee SM, Kang DS, Roh JS. Bulk graphite: materials and manufacturing process. *Carbon Lett*. 2015;16(3):135-146.
15. Gamson BW, Bailey BL. Graphite electrodes. *Ind Eng Chem*. 1954;46(1).
16. Surovtseva D, Crossin E, Pell R, Stamford L. Toward a life cycle inventory for graphite production. *J Ind Ecol*. 2022;26:964-979. Lci
17. Green Graphite Electrodes. Published 2022. Accessed June 15, 2022. https://www.coidan.com/green-graphite-electrodes
18. Tripathi N, Hills CD, Singh RS, Atkinson CJ. Biomass waste utilisation in low-carbon products: harnessing a major potential resource. *npj Clim Atmos Sci*. 2019;2(1):1-10.

19. Yang Q, Zhou H, Bartocci P, et al. Prospective contributions of biomass pyrolysis to China's 2050 carbon reduction and renewable energy goals. *Nat Commun*. 2021;12(1):1698.
20. Liao Y, Koelewijn SF, van Bossche den G, et al. A sustainable wood biorefinery for low-carbon footprint chemicals production. *Science*. 2020;367(6484):1385-1390. *(80-)*.
21. OYA A, MARSH H. Phenomena of catalytic graphitization. *J Mater Sci*. 1982;17(2):309-322.
22. Khoshk Rish S, Tahmasebi A, Wang R, Dou J, Yu J. Formation mechanism of nano graphitic structures during microwave catalytic graphitization of activated carbon. *Diam Relat Mater*. 2021;120:108699. November.
23. Kim YJ, Bae SW, Kim SH, Lim NS, Park SH. Effects of B and Ti addition and heat treatment temperature on graphitization behavior of Fe-0.55C-2.3Si steel. *J Mater Res Technol*. 2020;9(5):11189-11200.
24. Li H, Zhang H, Li K, Zhang J, Sun M, Su B. Catalytic graphitization of coke carbon by iron : understanding the evolution of carbon Structure, morphology and lattice fringes. *Fuel*. 2020;279(June):118531.
25. Sagues WJ, Yang J, Monroe N, et al. A simple method for producing bio-based anode materials for lithium-ion batteries. *Green Chem*. 2020;22(20):7093-7108.
26. Zhang C, Lu G, Sun Z, Yu J. Catalytic graphitization of carbon/carbon composites by lanthanum oxide. *J Rare Earths*. 2012;30(2):128-132.
27. Banek NA, Abele DT, McKenzie KR, Wagner MJ. Sustainable conversion of lignocellulose to high-purity, highly crystalline flake potato graphite. *ACS Sustain Chem Eng*. 2018;6(10):13199-13207.
28. Dhakate SR, Mathur RB, Bahl OP. Catalytic effect of iron oxide on carbon/carbon composites during graphitization. *Carbon NY*. 1997;35(12):1753-1756.
29. Yu J, Tian FJ, McKenzie LJ, Li CZ. Char-supported nano iron catalyst for water-gas-shift reaction: Hydrogen production from coal/biomass gasification. *Process Safety and Environmental Protection*. 2006;84(2):125-130.
30. Zhang N, Xian G, Li X, Zhang P, Zhang G, Zhu J. Iron based catalysts used in water treatment assisted by ultrasound: a mini review. *Front Chem*. 2018;6:1-6. February.
31. Sajitha EP, Prasad V, Subramanyam SV, Eto S, Takai K, Enoki T. Synthesis and characteristics of iron nanoparticles in a carbon matrix along with the catalytic graphitization of amorphous carbon. *Carbon NY*. 2004;42(14):2815-2820.
32. Vicente A de A S, Moreno JR, Santos TF de A, Espinosa DCR, Tenório JAS. Nucleation and growth of graphite particles in ductile cast iron. *J Alloys Compd*. 2019;775:1230-1234.
33. Theuwissen K, Lacaze J, Laffont L. Structure of graphite precipitates in cast iron. *Carbon NY*. 2016;96:1120-1128.
34. Synthetic Graphite Advanced Topics; Morphology. Published 2006. Accessed June 15, 2022. https://asbury.com/media/1227/syntheticgraphitepartii.pdf
35. Dunn JB, Gaines L, Barnes M, Wang M. Material and energy flows in the materials production, assembly, and end-of-life stages of the automotive lithium-ion battery life cycle. 2014
36. Hanhart V, Frankenstein L, Ramirez-Rico J, et al. Insights into the impact of activators on the 'catalytic' graphitization to design anode materials for lithium ion batteries. *ChemElectroChem*. 2022;9(21):e202200819.
37. Placke T, Siozios V, Rothermel S, Meister P, Colle C, Winter M. Assessment of surface heterogeneity: a route to correlate and quantify the 1st cycle irreversible capacity caused by SEI formation to the various surfaces of graphite anodes for lithium ion cells. *Zeitschrift fur Phys Chemie*. 2015;229(9):1451-1469.
38. Winter M, Novak P, Monnier A. Graphites for lithium - ion cells : the correlation of the first - cycle charge loss with the Brunauer - Emmett - Teller surface area graphites for lithium-ion cells : the correlation of the first-cycle charge loss with the Brunauer—Emmew-Teller Surface. *J Electrochem Soc*. 1998;145:428-436.
39. Adhikari S, Nam H, Chakraborty JP. *Conversion of solid wastes to fuels and chemicals through pyrolysis*. Elsevier B.V.; 2018.
40. Meng J, Moore A, Tilotta D, Kelley S, Park S. Toward understanding of bio-oil aging: accelerated aging of bio-oil fractions. *ACS Sustain Chem Eng*. 2014;2(8):2011-2018.
41. Babich A, Senk D. *Coal use in iron and steel metallurgy*. Woodhead Publishing Limited; 2013.
42. Cai J, Rahman M, Zhang S, et al. Review on aging of bio-oil from biomass pyrolysis and strategy to slowing aging. *Energy Fuels*. 2021;15:11665-11692. Published online.
43. Kurzweil P, Brandt K. *Overview of rechargeable lithium battery systems*. Elsevier B.V.; 2018.
44. Deraman M, Zakaria S, Omar R, Aziz AA. Electrical conductivity of carbon pellets from mixtures of pyropolymer from oil palm bunch and cotton cellulose. *Jpn J Appl Phys*. 2000;39(12A):L1236.
45. Dou X, Hasa I, Saurel D, et al. Hard carbons for sodium-ion batteries: structure, analysis, sustainability, and electrochemistry. *Mater Today*. 2019;23(March):87-104.

SUPPORTING INFORMATION

Additional supporting information can be found online in the Supporting Information section at the end of this article.

How to cite this article: Shi Z, Wang S, Jin Y, et al. Establishment of green graphite industry: Graphite from biomass and its various applications. *SusMat*. 2023;3:402–415.
https://doi.org/10.1002/sus2.139